A Self-Sustained Microwave System for Dielectric-Constant Measurement of Lossy Organic Liquids

Vikram Sekar, *Member, IEEE,* William J. Torke, *Student Member, IEEE,*
Samuel Palermo, *Member, IEEE*, and Kamran Entesari, *Member, IEEE*

Abstract—In this paper, dielectric constants of lossy organic liquids are measured using oscillation frequency shifts of a negative-resistance voltage-controlled oscillator (VCO). The design and working principle of the oscillator and the effect of material loss are presented in detail. The proposed method provides relatively large frequency shifts of 10–110 MHz for lossy test sample volumes of 50–200 μL whose dielectric constants are between 2–13 at 4.5 GHz, thereby allowing good resolution in dielectric-constant measurement. To make the system self-sustained, the VCO is used as part of a frequency synthesizer system for frequency-to-voltage conversion and digital extraction of the frequency shift using a unique detection algorithm. The dielectric constant of several organic liquids have been extracted to an accuracy better than 2% using sample volumes of 50–200 μL, and has excellent agreement with reported values. The applicability of this system for sensing dielectric mixtures has also been shown, and volume fraction estimation has been demonstrated to an accuracy of around 1%.

Index Terms—Dielectric-constant measurement, dielectric mixture, frequency synthesizer, negative resistance oscillator, split-ring resonator (SRR).

I. INTRODUCTION

T HE development of highly accurate systems for detection of dielectric constant of a material has numerous applications in agriculture, industry, and medicine. Estimation of moisture content in grain and timber are of vital importance in industry [1], [2]. In medicine, biological tissues have been characterized using microwave permittivity measurements [3]. Measurement of dielectric properties of chemicals, polymers, and gels provide important information regarding their chemical composition and structure [4].

Microwave techniques employing waveguide resonators are based on resonant frequency and Q-factor changes due to field perturbations induced by the material-under-test (MUT), and they are capable of accurate permittivity measurements at a single frequency or discrete set of frequencies [5]. Such sensors are often bulky and expensive when low-cost *in situ* material measurements need to be performed. In comparison, substrate-integrated-waveguide resonators and planar microstrip resonators provide a low-cost compact alternative for permittivity measurement, although with lower sensitivities [6], [7]. However, these approaches are based on measuring relative changes in the maximum or minimum values of the S-parameter magnitude response ($|S_{21}|$ or $|S_{11}|$) in the presence of the MUT. For a MUT with high loss, severe degradation of the resonator Q factor makes the peak or notch in the S-parameter response completely disappear, thereby making it impossible to extract the permittivity of the MUT. To detect high-loss materials using this technique, the sample volume of the lossy MUT is greatly reduced to lower resonator loading and maintain a relatively high resonator Q factor. As a result, the resonant frequency shifts caused by the MUT significantly reduce, making it hard to estimate the dielectric constant accurately.

For portable applications, the need for laboratory equipment must be eliminated. Several approaches have been demonstrated to make the permittivity measurement system completely self-sustained. In [8], frequency sweep generators and power detectors are used to digitally obtain the shift in $|S_{21}|$ response of a planar resonator, and obtain the properties of the MUT through Lorentzian fitting. In [9], a phase-locked loop (PLL) is employed where the reflected and transmitted signals through the resonator are used for permittivity measurements. Here, the system operates by adjusting the frequency of the voltage-controlled oscillator (VCO) to match the resonant frequency of the sensor until no energy is reflected from the sensor. Both these systems rely on the peak or notch in the magnitude S-parameter response of the resonator, making it unsuitable for the measurement of high-loss MUTs.

In this paper, a self-sustained approach is presented to accurately measure dielectric constant using a negative-resistance VCO embedded in a frequency synthesizer system. Section II discusses the proposed technique, which relies on the change in phase response of a planar sensor present in the gate network of a VCO and the corresponding change in oscillation frequency for detection of dielectric constant. The dependence of the system on phase response allows the use of lossy test sample
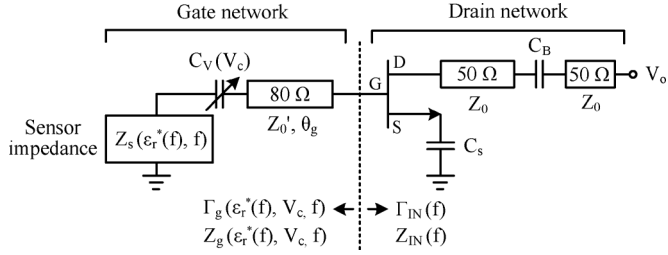
Fig. 1. Simplified schematic of the negative resistance oscillator used for permittivity measurement.

volumes up to 200 μL, while maintaining stable oscillations. This provides large frequency shifts and enables improved resolution for dielectric-constant measurement. By employing a frequency synthesizer system detailed in Section III, the oscillation frequency shift is converted to a voltage shift. Using a microcontroller unit (MCU) with an integrated analog-to-digital converter (ADC), the voltage shift is used to digitally obtain the change in oscillation frequency through a unique detection algorithm. Section IV reports measured chemical calibration and detection results, and since measurement of dielectric constant alone is enough to distinguish and quantify mixtures [6], the application of this system is also demonstrated to detect the composition of a mixture of organic liquids. Finally, Section V concludes this paper.

II. OSCILLATORS FOR DIELECTRIC-CONSTANT MEASUREMENT

A. Oscillator Design

Fig. 1 shows the schematic of a negative resistance oscillator employing a source series feedback capacitance (C_s) to generate negative resistance. The gate network has a transmission line with characteristic impedance $Z_0' = 80$ Ω and electrical length θ_g in series with a voltage-controlled varactor $C_v(V_c)$ and a sensing element with complex impedance $Z_s(f)$. When a MUT with complex frequency-dependent relative permittivity $\epsilon_r^*(f) = \epsilon_r'(f) - j\epsilon_r''(f)$ is applied to the sensor, its impedance changes as $Z_s(\epsilon_r^*(f), f)$. Here, $\epsilon_r'(f)$ and $\epsilon_r''(f)$ depict the dielectric constant and loss of the MUT, respectively. In general, the oscillation frequency depends on the variable loads in the gate network, which, in this case, are $C_v(V_s)$ and $Z_s(\epsilon_r^*(f), f)$, respectively. The purpose of the varactor is to negate any changes in oscillation frequency caused by the MUT. The oscillating signal is available at the output of the drain network, which has two transmission lines of arbitrary electrical length (with characteristic impedance $Z_0 = 50$ Ω) with a dc blocking capacitor C_B between them.

1) Source Network: To design an oscillator with an output frequency of f_0, the value of C_s must be adjusted so that the transistor provides a negative resistance looking into the gate, implying $|\Gamma_{IN}(f_0)| > 1$. To determine the value of C_s, the S-parameters of a properly biased transistor, terminated by 50-Ω loads at the gate and drain [see Fig. 2(a)] are simulated in
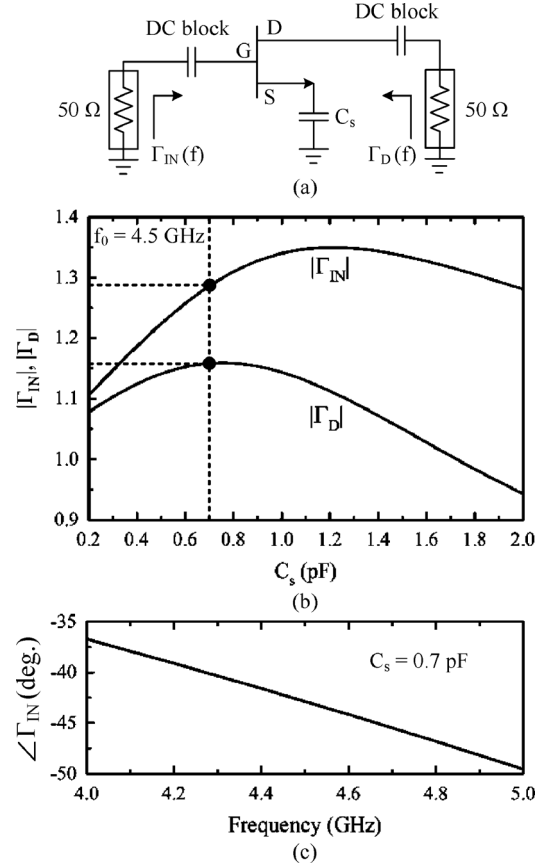

Fig. 2. (a) Simulation setup for the determination of C_s (dc biasing not shown). (b) Variation of magnitude of reflection coefficients at gate and drain with C_s. (c) Phase variation of gate reflection coefficient with frequency.

Agilent ADS[1] using the nonlinear model of the transistor. The active device is an Avago Technologies' ATF-36077 pseudomorphic high electron-mobility transistor (pHEMT) biased at a drain–source voltage (V_{DS}) of 1.5 V and gate–source voltage (V_{GS}) of -0.2 V with a drain current (I_D) of 10 mA.

Fig. 2(b) shows the variation of $|\Gamma_{IN}|$ and $|\Gamma_D|$ at $f_0 = 4.5$ GHz when different values of C_s are connected to the source terminal of the transistor. To measure high-loss MUTs, the negative resistance generated must be maximum to ensure stable oscillations. Thus, the value of C_s must be chosen so that the magnitude of reflection coefficients at the gate and drain are maximized. Choosing $C_s = 0.7$ pF results in $|\Gamma_{IN}| = 1.29$ and $|\Gamma_D| = 1.16$. Fig. 2(c) shows the variation of $\angle\Gamma_{IN}$ with frequency for $C_s = 0.7$ pF. For stable oscillations at a frequency f_0, the gate network must be designed to meet the following conditions [10]:

$$|\Gamma_{IN}(f_0)| \times |\Gamma_g(\epsilon_r^*, V_c, f_0)| > 1 \qquad (1)$$
$$\angle\Gamma_g(\epsilon_r^*, V_c, f_0) = -\angle\Gamma_{IN}(f_0). \qquad (2)$$

Since the overall network looking into the gate is capacitive, the gate network should be made inductive to satisfy the oscillation condition given by (2).

2) Gate Network: The sensing element is a split-ring resonator (SRR) coupled to a microstrip line, as shown in Fig. 3(a).

[1]Agilent Technologies' Advanced Design System (ADS), Palo Alto, CA, 2006.
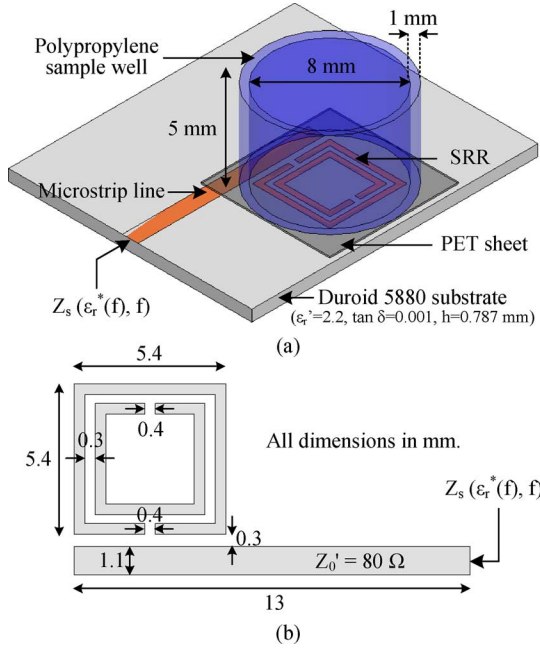
Fig. 3. (a) 3-D view of the sensing element. (b) Dimensions of the SRR.

The high confinement of electric fields at the open ends and be-tween the rings of the SRR makes it highly sensitive to per-mittivity changes in the dielectric layer above it [11]. The SRR is covered by a 100-μm-thick sheet of polyethylene terapha-late (PET) with $\epsilon_r = 2.5$ and $\tan \delta = 0.025$ to prevent the sensor metallization from degrading when the MUT is applied. In order to contain the MUT, a sample well is constructed using a 5-mm-long polypropylene tube ($\epsilon_r = 2.2$) with a wall thick-ness of 1 mm and inner diameter of 8 mm.

The dimensions of the SRR are shown in Fig. 3(b) and are chosen such that the SRR has an arbitrary resonant frequency that is above the desired oscillation frequency. This makes the SRR appear inductive at the oscillation frequency, as required by the gate network [12]. As a result, any phenomena induced by the MUT at frequencies close to the resonant frequency of the SRR do not affect the performance of the sensing oscillator. The sensing element is simulated using Ansoft HFSS[2] to find the value of Z_s at $f_0 = 4.5$ GHz when the MUT is absent. On account of the SRR-to-microstrip coupling and the 13-mm-long transmission line with an 80-Ω characteristic impedance, the sensing element appears capacitive with an impedance $Z_s(\epsilon_r^* = 1, f_0) = 1.2 - j40 \ \Omega$.

The varactor in Fig. 1 is a silicon-hyperabrupt tuning varactor from Aeroflex/Metelics (MHV500) that provides a capacitance of $C_{v0} = C_v(V_c = 0 \ \text{V}) = 2.5$ pF. Neglecting varactor para-sitics for simplicity, the equivalent input impedance of the gate network when $V_c = 0$ V is given by

$$Z_g(f) = Z_0' \frac{Z_s(\epsilon_r^*(f), f) + j \left(Z_0' \tan \theta_g - \dfrac{1}{2\pi f C_{v0}} \right)}{\left(Z_0' + \dfrac{\tan \theta_g}{2\pi f C_{v0}} \right) + j Z_s(f) \tan \theta_g} \quad (3)$$
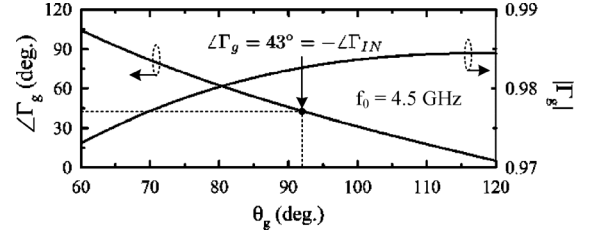
Fig. 4. Magnitude and phase variation of reflection coefficient of the gate net-work as a function of the electrical length of the gate transmission line.

and the complex gate reflection coefficient is given by

$$\Gamma_g \left(\epsilon_r^*(f), V_c = 0, f \right) = \frac{Z_g(f) - Z_0}{Z_g(f) + Z_0}. \quad (4)$$

For an oscillation frequency of $f_0 = 4.5$ GHz in the ab-sence of a MUT when $V_c = 0$ V, the electrical length θ_g of the transmission line in the gate network should be chosen so that (1) and (2) are satisfied. Assuming a sensor impedance of $Z_s(\epsilon_r^* = 1, f_0)$, $|\Gamma_g|$ and $\angle \Gamma_g$ can be calculated using (3) and (4). Fig. 4 shows the variation of $\angle \Gamma_g$ for different values of θ_g. Choosing $\theta_g = 92°$ results in $\angle \Gamma_g = 43° = -\angle \Gamma_{\text{IN}}$ at 4.5 GHz. The simulated values of $|\Gamma_g|$ are close to unity, and hence, sat-isfy the condition in (1). The oscillator design is now complete. The response of the oscillator to MUT dielectric constant and effect of MUT loss is described below.

B. Response to Material Dielectric Constant

To examine the effect of material dielectric constant (ϵ_r') on the oscillator, the impedance of the sensing element, $Z_s(\epsilon_r', f)$, is simulated in HFSS with lossless isotropic MUTs of various di-electric constants present in the sample well. It is assumed that the dielectric constant is frequency independent and the sample well is completely filled with the MUT, to a height of 5 mm above the SRR. From the simulated values of $Z_s(\epsilon_r', f)$, the phase variation of the gate reflection coefficient [$\angle \Gamma_g(\epsilon_r', V_c = 0, f)$] is calculated using (3) and (4) for each ϵ_r', as shown in Fig. 5(a). Negated phase variation of the reflection coefficient looking into the gate of the transistor [$\angle \Gamma_{\text{IN}}(f)$ from Fig. 2(c)] is also superimposed. The points of intersection between these curves are the frequencies at which the oscillation condition given by (2) is satisfied and determine the oscillation frequen-cies for each value of ϵ_r'. The relative percentage change of the oscillation frequency as a function of MUT dielectric con-stant is shown in Fig. 5(b). The effective capacitance (C_ϵ) of the sensing element extracted from $Z_s(\epsilon_r', f)$ is also shown and has higher values as ϵ_r' of the MUT increases. Thus, determining the change in oscillation frequency is an effective means to es-timate the dielectric constant of the MUT.

For lossless MUTs ($\epsilon_r'' = 0$), the real part of sensor impedance Z_s remains unchanged with a value of 1.2 Ω, which is mostly attributed to metallic losses in microstrip traces and dielectric losses in the Duroid substrate, polyethylene sample well, and PET sheet. Hence, the oscillation condition given by (1) is met for all values of ϵ_r' since $|\Gamma_g| \approx 1$, as shown in Fig. 4, en-suring sustained oscillations at frequencies that only depend on the MUT dielectric constant.
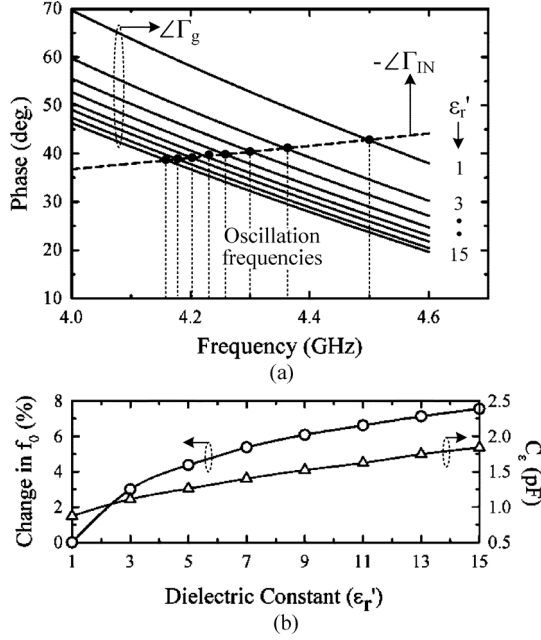
Fig. 5. Simulated: (a) phase of reflection coefficient of the gate network caused by the presence of MUTs. (b) Change in oscillation frequency and effective sensor capacitance versus dielectric constant.

C. Effect of Material Loss

When a MUT with loss ($\epsilon_r'' \neq 0$) is present above the SRR, the sensing element is equivalently represented by a *lossy* capacitor whose admittance is given by

$$Y_s(\epsilon^*(f), f) = \frac{1}{Z_s(\epsilon^*(f), f)} = G_\epsilon + j\omega C_\epsilon. \qquad (5)$$

where G_ϵ is a conductance that depends only on the ϵ_r'' of the MUT. Fig. 6(a) shows the relatively linear increase of G_ϵ with ϵ_r'' at $f_0 = 4.5$ GHz, obtained from full-wave simulation of the sensing element in HFSS in the presence of lossy materials. Here, ϵ_r'' is assumed to be frequency independent and the lossy material is assumed to fill the sample well to a height of 5 mm. Simulations also verify that the extracted conductance values are independent of ϵ_r' and remain almost constant in a narrow bandwidth ($\approx 20\%$) of frequencies around f_0. The oscillation frequencies calculated from (2) also show that they are independent of material loss. This is because the shift in oscillation frequency relies only on the phase change induced by the change in sensing capacitance since ϵ_r' and ϵ_r'' affect the real and imaginary parts of the sensing admittance, respectively, and measurement of ϵ_r' is completely independent of ϵ_r''. However, the conductance G_ϵ may impose restrictions on the capability for sustained oscillations.

To ensure sustained oscillations in the presence of a lossy material, the oscillation condition in (1) must be satisfied for all values of ϵ_r' and ϵ_r''. Fig. 6(b) and (c) shows the simulated product of $|\Gamma_{IN}|$ and $|\Gamma_g|$ as a function of ϵ_r'' for different values of ϵ_r' for constant oscillation frequency and constant varactor voltage cases, respectively. It is important to maintain sustained oscillations for both these cases to ensure proper operation of the detection algorithm, as explained in Section III. In the constant frequency case, the varactor voltage V_c is adjusted to maintain a constant oscillation frequency of 4.5 GHz for each value of
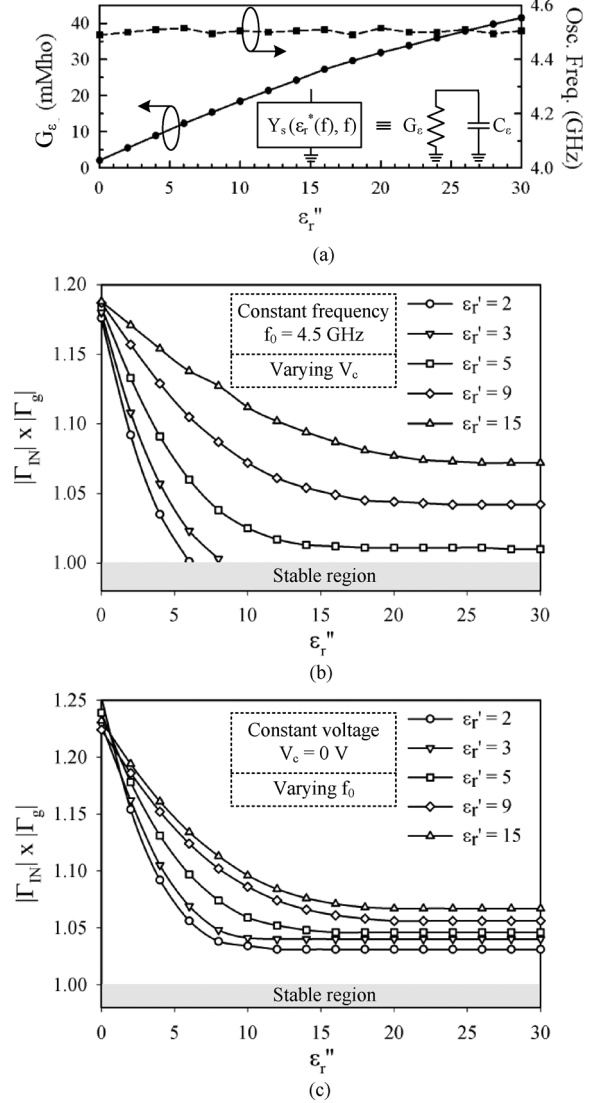

Fig. 6. Simulated: (a) real part of sensor admittance when lossy isotropic MUTs with $\epsilon_r' = 1$ and various ϵ_r''-values are placed in the sample well. Oscillation condition in (1) as a function of ϵ_r'' for the case of (b) constant oscillation frequency and (c) constant varactor voltage.

ϵ_r'. In the constant voltage case, the varactor voltage is constant ($V_c = 0$ V) and the oscillation condition is calculated at the frequency of oscillation corresponding to the value of ϵ_r' [see Fig. 5(c)].

When $|\Gamma_{IN}| \times |\Gamma_g| < 1$, the oscillator enters a stable mode of operation and cannot maintain sustained oscillations. Thus, for a given ϵ_r', there is a maximum limit on the range of ϵ_r'' beyond which the oscillator does not oscillate. Fig. 6(b) shows that stable oscillations are supported for a wide range of ϵ_r'' values for high ϵ_r'. For low ϵ_r' values, the oscillator enters the stable region, thereby limiting the range of ϵ_r'' that can be detected. This restriction occurs only when the low ϵ_r' materials have loss tangents ($\tan\delta = \epsilon_r''/\epsilon_r'$) in the range of 2.5–3, which is a very high value for most organic liquids in the gigahertz range [13]. Material loss does not restrict oscillations for the constant voltage case, as shown in Fig. 6(c). Hence, this oscillator guarantees sustained oscillations for a wide range of practical materials that need to be tested.
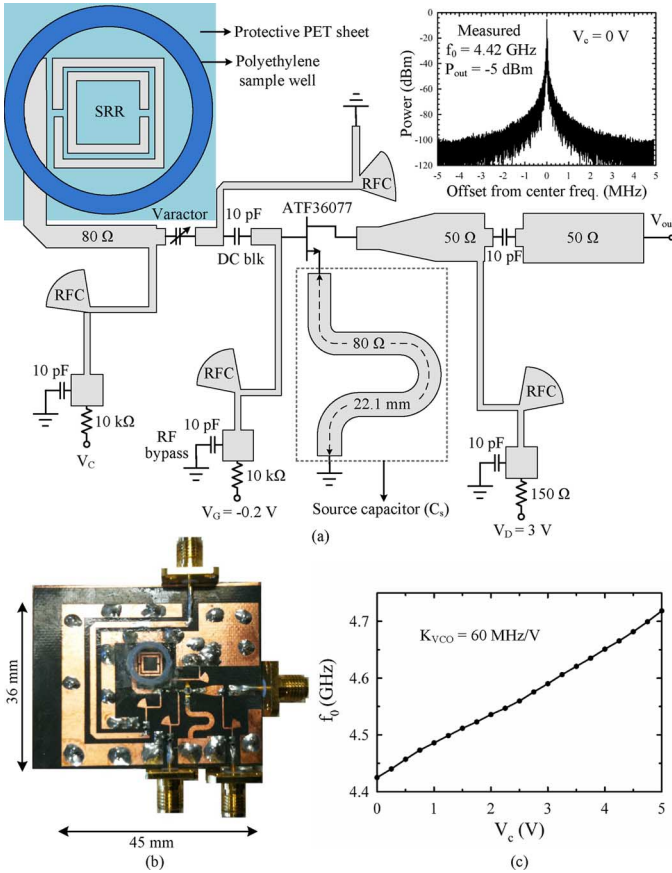
Fig. 7. (a) Detailed layout of the negative resistance VCO for dielectric-constant measurement. Measured frequency response is also shown. (b) Fabricated VCO prototype. (c) Measured VCO tuning characteristic.

D. Implementation

Fig. 7(a) shows the detailed layout of the VCO on a 0.787-mm-thick RT/Duroid 5880 substrate ($\epsilon_r = 2.2$, $\tan\delta = 0.0009$). The source capacitor ($C_s = 0.7$ pF) is implemented using an 80-Ω short stub with an electrical length of 302°, and is meandered to minimize its area. The microstrip line of the sensing element is bent into an L-shape to minimize area, and the parasitics associated with the bend are included in full-wave simulation. The polypropylene sample well is glued onto the protective PET sheet, which is then centered over the SRR and firmly attached to the VCO board. Care must be taken to reduce the air gap between the SRR and PET sheet since it can decrease the sensitivity of the VCO to the MUT.

The equivalent models of the varactor (Aeroflex/Metelics MHV500),[3] dc blocking and RF-bypass capacitors, biasing resistors[4] and nonlinear model of the pHEMT transistor (Avago Technologies' ATF36077) are used in VCO co-simulation using Agilent ADS and Momentum. DC block and RF bypass capacitors are AVX Accu-P 10-pF capacitors (0402 size) while biasing resistors are Vishay thick-film resistors (0402 size) with values of 150 Ω and 10 kΩ. RF chokes (RFCs) are implemented using fan-stubs connected to quarter-wavelength

[3]Aeroflex/Metelics MHV500 silicon hyperabrupt tuning varactor datasheet. [Online.] Available: www.aeroflex.com

[4]Modelithics Inc., passive component (CLR) library, Tampa, FL, 2011.

high-impedance transmission lines. The overall length of the transmission lines in the gate network are adjusted using full-wave simulations to meet the oscillation conditions at 4.5 GHz, as described in Section II-A.

Fig. 7(b) shows the fabricated VCO prototype. The measured oscillation spectrum in the absence of MUT has a center frequency of $f_0 = 4.42$ GHz and output power of $P_{\text{out}} = -5$ dBm when $V_c = 0$ V. Fig. 7(c) shows the tuning characteristic of the VCO with varactor voltage V_c, which exhibits a tuning slope of $K_{\text{VCO}} = 60$ MHz/V and a total tuning range of 300 MHz. Detailed measurements of the VCO response to organic liquids are reported in [12]. To make the system self-sustained, the VCO is embedded in a frequency synthesizer system to convert oscillation frequency shifts to voltages, and is described below.

III. FREQUENCY SYNTHESIZER SYSTEM

A. Functionality

A functional block diagram of the frequency-shift measurement system is shown in Fig. 8 [20]. The system consists of a PLL-based frequency synthesizer core along with ADC and an MCU. The ADC is used to digitally sample the loop filter output or equivalently the control voltage to the oscillator V_c. The purpose of the MCU is to administer the frequency-shift measurement process and to provide a digital communication interface between the measurement system and a PC. The VCO block within the PLL is the planar microwave VCO with SRR-based sensing element described in Section II. The purpose of the frequency synthesizer system is to calculate the shift in oscillation frequency exhibited by the VCO due to the dielectric constant (ϵ_r') of the MUT.

The sequence of steps involved in frequency-shift measurement is graphically illustrated in Fig. 9(a) and is tabulated in Fig. 9(b). The measurement process consists of three phases.

1) Initialization: The programmable frequency divider is initially set to a value N_0 so that the frequency synthesizer is locked to a frequency $f_0 = 4.48$ GHz with no MUT applied. The MCU digitally records the control voltage level at this time, which is denoted by V_{c1}.

2) Detection: A known volume of the MUT is dispensed into the sample well of the VCO. Although the oscillation frequency of the VCO initially decreases, the PLL returns to the locked state and maintains the output frequency at f_0 by increasing the control voltage to the oscillator from V_{c1} to V_{c2}. The voltage V_{c2} is then digitally sampled and stored in the MCU. From Fig. 6(b), oscillation is guaranteed for the constant frequency transition between phases 1 and 2 for most practical materials.

3) Calculation: Using a binary search algorithm, the MCU digitally alters the frequency division value from N_0 to N_1 so that the oscillator control voltage returns from a value V_{c2} to its approximately original value, V_{c1}, limited by the quantization error of the frequency divider. As a result, the output frequency of the synthesizer system changes from f_0 to f_1. The oscillation frequency shift Δf caused by the MUT is then computed as $\Delta f = f_0 - f_1 = (N_1 - N_0)f_{\text{ref}}$. From Fig. 6(c), oscillation is guaranteed for the constant voltage transition between phases 1 and 3. Since oscillation is guaranteed at phases 2 and 3, stable oscillations are obtained at all voltages (and frequencies)
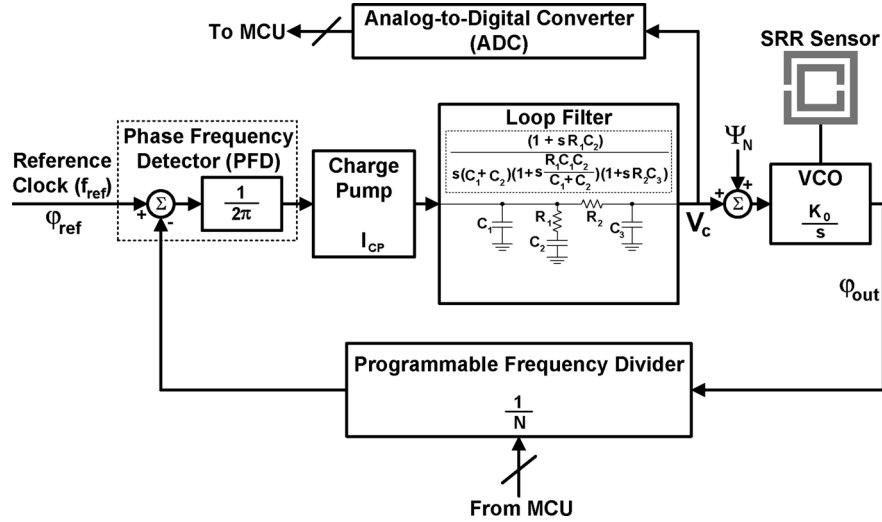
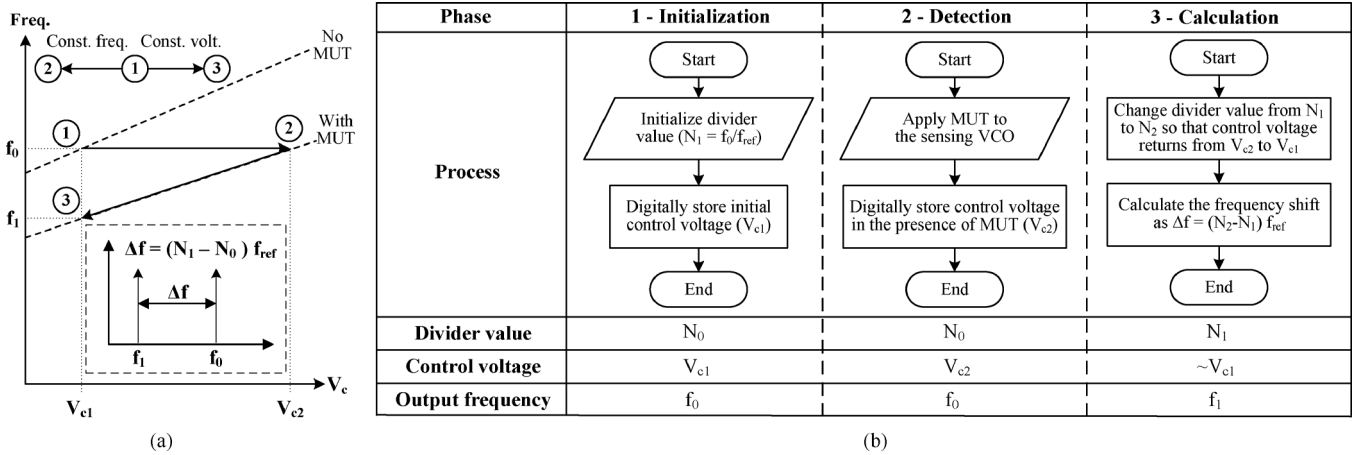Fig. 8. Block diagram of the frequency-shift measurement system used for dielectric-constant measurement.

Fig. 9. (a) Graphical illustration and (b) detailed description of the frequency-shift measurement procedure.

between V_{c1} and V_{c2} (and between f_0 and f_1) for the transition between phases 2 and 3.

B. System Implementation

The measurement system pictured in Fig. 10 is realized as a discrete electronic system constructed on two separate printed circuit board (PCB) assemblies, i.e.: 1) the "VCO Board" contains the negative resistance oscillator with planar microwave SRR sensor, as described in Section II and 2) all remaining system components occupy a second PCB of 62-mil-thick FR4 substrate, referred to as the "PLL Board." A block level diagram of the PLL Board is shown in Fig. 11. The RF output of the VCO Board is fed to a fractional-N frequency synthesizer integrated circuit (IC) [14], which provides 25-bit resolution fractional-N division. This extremely high resolution of the loop division factor allows for precise frequency-shift measurements by minimizing the quantization error that occurs when the control voltage is returned to the original V_{c1} level measured before MUT introduction. In addition to the programmable frequency divider, the frequency synthesizer IC also contains the phase-frequency detector (PFD) and charge pump blocks. The charge pump output is fed to a passive loop filter comprised of discrete R and C components. The output from this loop filter

is V_c, which is fed back to the VCO Board assembly, thereby completing the frequency synthesizer loop.

Fig. 11 shows that the loop filter output voltage is also connected to the input of a unity gain buffer comprised of a dual low-noise op-amp IC to allow for digital sampling of V_c. This buffer provides a replica of the V_c while presenting minimal loading to the actual loop filter output. The buffered version of V_c is then passed through a simple resistive divider with a ratio of $R = 0.672$ to scale the 5-V dynamic range of the loop filter output to within the 3.25-V maximum dynamic range of the ADC input. Before being presented to the ADC input, this buffered and scaled version of V_c is passed through a single-pole Butterworth antialiasing filter. The ADC sampling frequency was set to the highest possible value (250 kHz), the primary constraint being the MIPs bandwidth required by the MCU firmware to process and then store each successive ADC sample. The -3-dB cutoff frequency of the antialiasing filter was therefore set to the Nyquist frequency of 125 kHz.

The 16-bit ADC is an integrated peripheral within the MCU device [15]. Firmware was developed for this MCU to administer various system-level tasks, including configuration of the frequency synthesizer device (via three-wire serial interface), the frequency measurement process, as well as universal asynchronous receiver/transmitter (UART) functionality. The
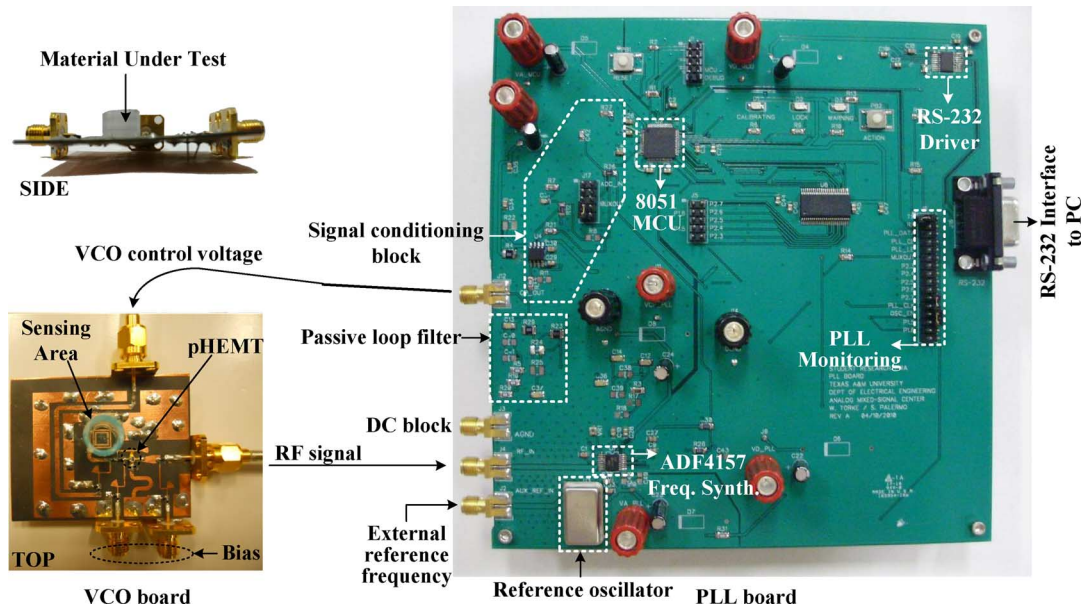
Fig. 10.   Photograph of the frequency synthesizer system for dielectric-constant measurement.
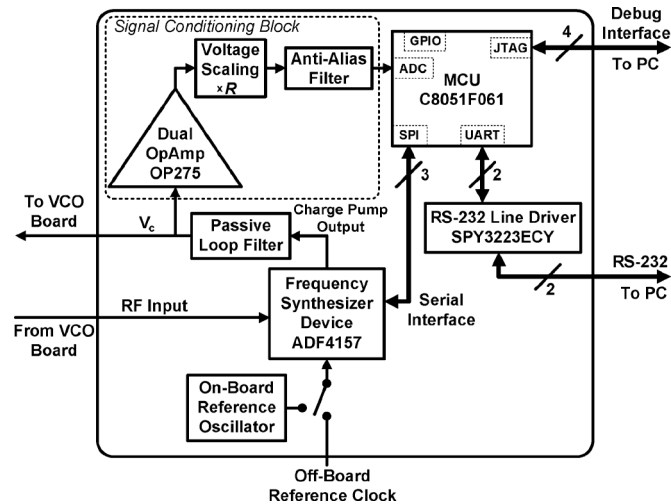

Fig. 11.   Block-level diagram of PLL board.

UART functionality supports an off-board interface through an RS-232 line driver IC so that the PLL Board assembly can be connected to a PC. A control/interface software application was developed for the PC platform using National Instruments' LabView,[5] which utilizes this RS-232 interface. This software application can transmit various commands to the MCU to allow for initiation of the various system-level tasks by the user, and to provide an on-screen panel in which the frequency-shift measurement results (as well as various other configurable system-level parameters) can be displayed.

Note that the debug interface shown in Fig. 11 is used only for writing the firmware object code to the MCU, and for debug of the firmware. It is not used for any frequency measurement purpose.

The PLL Board is powered via connection of a $+3.25$-V power supply along with $+/-5$-V supplies. The reference

clock can be provided either from an on-board high-precision low-drift canned oscillator or from an external signal source.

C. PLL Design Considerations

A linear phase model of the PLL can be constructed using the s-domain parameters indicated within the various individual PLL blocks pictured in Fig. 8. As the primary function of this PLL is to represent a shift in the VCO's oscillation frequency by a corresponding shift in the loop filter output voltage, highest priority in the design was devoted to minimization of noise at the loop filter output. It is reasonable to assume that VCO phase noise is the dominant loop noise source, in comparison to phase noise originating from the reference clock source, which is provided either from a signal generator or a very stable crystal-based canned oscillator. The VCO noise can be modeled as an additional voltage source, Ψ_N, referred to the VCO input, as shown in Fig. 8. The transfer function from the VCO input referred voltage noise to V_c is given by the low-pass expression of (6). In this equation, $K_0 = 2\pi K_{\text{VCO}}$.

Based on typical VCO phase-noise profiles, the amount of noise at V_c originating from VCO phase noise can be reduced by minimizing the PLL loop bandwidth in this sensor system. Note this low-bandwidth design choice is in contrast to traditional PLL frequency synthesizer design practices, where a relatively low loop bandwidth will generally cause increased VCO phase-noise contribution to the output clock signal [19]. Fast settling time is also not a priority for this chemical sensing application, as the control voltage is sampled only during steady-state periods when the loop has stabilized, before or after MUT application.

The PLL was designed with a targeted 55° phase margin and ~ 23-kHz bandwidth, which balances VCO phase-noise filtering for adequate sensitivity and proper loop settling while incrementing the division ratio in the binary search algorithm to avoid long frequency-shift measurement calculation times [20]. While the sensor is in use, the loop bandwidth can subsequently

TABLE I
PLL DESIGN PARAMETERS

Output frequency	4.48 GHz (nominal)
Ref. frequency	14.86453 MHz
Freq. division ratio (N_0)	301.5 (nominal)
Loop bandwidth	23 kHz
Charge pump current (I_{CP})	5 mA
Settling time (to $< 1°$)	395 μs
Phase Margin	55 °
R_1	185 Ω
R_2	718 Ω
C_1	7.3 nF
C_2	185 nF
C_3	1.8 nF
K_{VCO}	60 MHz/V

Fig. 13. Measured transient response of control voltage for frequency step response from 4.480 to 4.775 GHz.
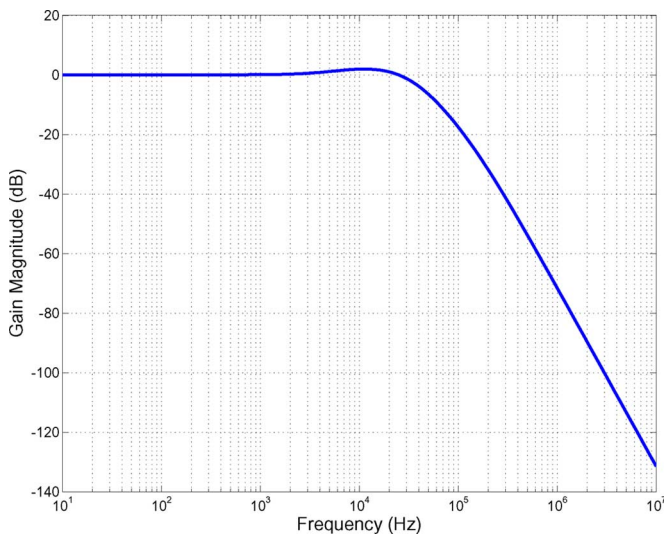

Fig. 12. Bode plot of VCO phase noise $\Psi_N(s)$ to $V_c(s)$ transfer function.

be lowered even further with relative ease by decreasing the charge pump current setting of the PLL device.

Since the PLL device is configured to achieve the fractional-N division by means of a second-order sigma–delta interpolator, a third-order loop filter was implemented to assist in the noise shaping of the sigma–delta spectrum [14]. The critical loop parameters are provided in Table I.

A bode plot of the transfer function from the input VCO noise source $\Psi_N(s)$ to $V_c(s)$ is shown in Fig. 12, when the final PLL parameter and component values are applied to (6) at the bottom of this page. It can be seen that the transfer function has a low-pass characteristic, and the bandwidth is close to the targeted loop bandwidth.

Fig. 13 shows the measured transient behavior of V_c in response to a 0.295-GHz step in frequency. The settling time
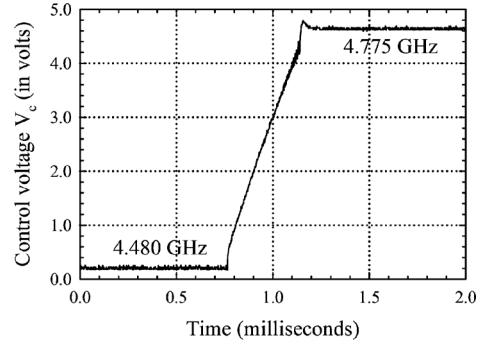
closely matches the simulated settling time of 395 μs. The pictured frequency step nearly spans the entire PLL lock range.

IV. MEASUREMENTS

A. Procedure

First, the MCU is initialized by the PC through the RS-232 serial interface and Labview VI. The MCU firmware then initializes the ADF4157 frequency synthesizer chip by programming the frequency divider value to $N_0 = f_0/f_{\text{ref}} = 4.48$ GHz/14.86086 MHz ≈ 301 so that an output frequency of f_0 is obtained when the PLL is in the locked state. When the loop is locked, the output of the loop filter has a voltage $V_{c1} \approx 1$ V, which is digitized by the ADC, averaged 2^{16} times by the MCU and stored in memory.

Second, a known sample volume of organic liquid to be analyzed is dispensed into the sample well of the VCO using a Finnpipette II single-channel pipetter[6] with adjustable volumes between 10–100 μL (accuracy $> 99\%$). To maintain locked state at a frequency f_0, the loop filter output voltage changes from V_{c1} to V_{c2}, which is then digitally averaged 2^{16} times by the MCU and stored in memory.

Finally, when the calculation phase is initiated, the MCU increases the divider value to a value N_1 so that the average loop filter output returns from V_{c2} to V_{c1}, and calculates the frequency shift $\Delta f = (N_1 - N_0)f_{\text{ref}}$. The result is conveyed to the PC and displayed on the monitor. The sample well is then dried completely using a cotton swab to remove excess material and a fan to accelerate evaporation before the next test.

B. Volume Sensitivity

To characterize the frequency shift provided by the system as a function of sample volume (S_v), volumes from 10 to 200 μL of

[6][Online.] Available: http://www.thermoscientific.com

$$\frac{V_c}{\Psi_N(s)} = -\frac{K_0 I_{CP}(1 + sR_1C_2)}{s^4 2\pi N R_1 R_2 C_1 C_2 C_3 + s^3 2\pi N[(C_1+C_2)R_2C_3 + R_1C_1C_2] + s^2 2\pi N(C_1+C_2) + sK_0 I_{CP}R_1C_2 + K_0 I_{CP}} \tag{6}$$
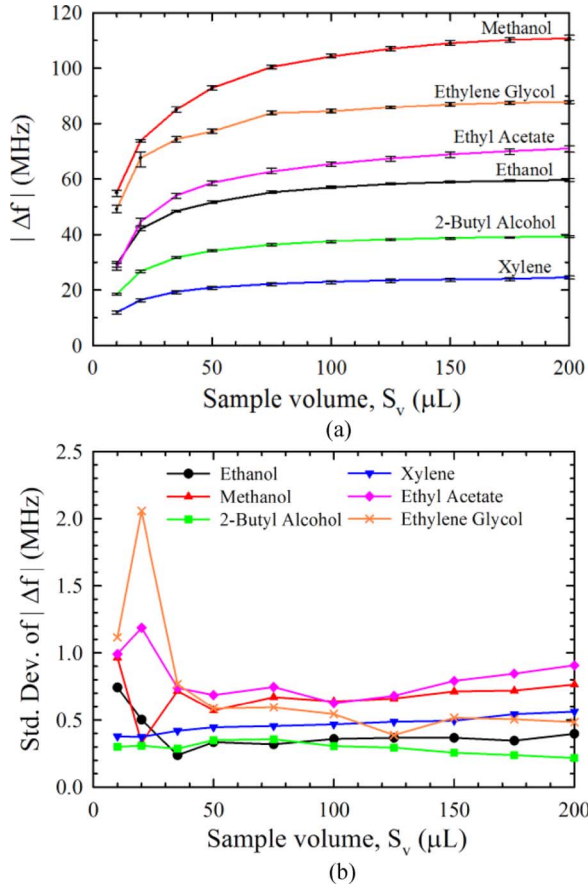
(a)

(b)

Fig. 14. (a) Measured frequency shift and (b) standard deviation of frequency shift, as a function of sample volume.

Fig. 15. Curve-fit calibration curves for various sample volumes.

various MUTs are dispensed into the sample well and frequency shifts are measured. For each sample volume of each MUT, five frequency measurements are taken and average frequency shifts are computed as shown in Fig. 14(a). The error bars are also indicated.

For any MUT, the average frequency shift increases with sample volume up to a certain value, and remains relatively constant thereafter. At low sample volumes ($< \approx 50\ \mu L$), a considerable part of the SRR fringing field extends above the MUT. Hence, frequency shift increases with sample volume due to greater interaction of the sensor electromagnetic field with the MUT. When the fringing field of the SRR is completely occupied by the MUT at large sample volumes, frequency shift becomes a weak function of sample volume.

Fig. 14(b) shows the standard deviation of frequency measurements over five trials for each MUT. For low sample volumes ($< \approx 35\ \mu L$), the standard deviation of frequency shift is higher due to insufficient coverage of the sensor electromagnetic field by the MUT, and errors in the sample volume dispensed. For larger sample volumes ($\geq 35\ \mu L$), the standard deviation of frequency shift is < 1 MHz due to complete coverage of the sensor field by the MUT and relative insensitivity of frequency shift to sample volumes.

C. Chemical Calibration and Detection

To calibrate the system for dielectric-constant measurement, ethanol and methanol are used as reference materials since
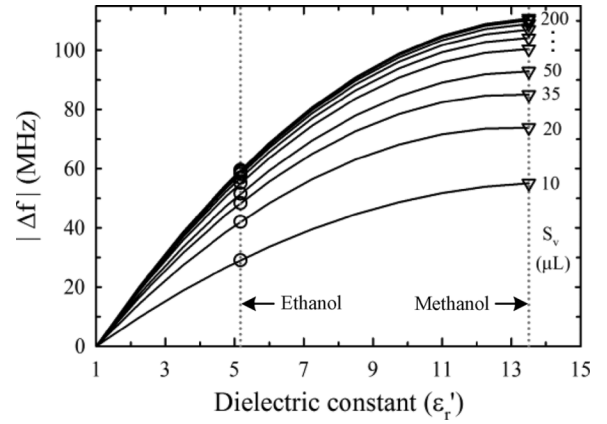
their properties are well known over frequency and temperature [16]. The calibration process imposes a reference for system response due to interaction between the inhomogeneous dielectric medium and the electromagnetic field of the SRR. Using the frequency shifts in the presence of air ($\epsilon'_r = 1$, $\Delta f = 0$), ethanol ($\epsilon'_r = 5.17$ @ 4.5 GHz and 20 °C), and methanol ($\epsilon'_r = 13.53$ @ 4.5 GHz and 20 °C), a curve-fit equation relating frequency shift ($|\Delta f|$) to ϵ'_r is obtained for a particular sample volume, S_v. The general representation of this curve-fit equation is a second-order polynomial expressed as

$$|\Delta f(S_v)| = a(S_v)\epsilon'^2_r + b(S_v)\epsilon'_r + c(S_v) \qquad (7)$$

where $a(S_v)$, $b(S_v)$, and $c(S_v)$ are coefficients that depend on the sample volume under test. Fig. 15 shows the curve-fit polynomials for sample volumes from 10 to 200 μL obtained from average frequency shift values of ethanol and methanol. The mean values of calibration coefficients and their measurement uncertainties for the various sample volumes are shown in Table II. Calibration coefficients are calculated by curve-fitting five polynomial curves corresponding to five frequency-shift measurements obtained for both ethanol and methanol, respectively. Uncertainty values represent the maximum deviation of calibration coefficients from their respective mean values. For low sample volumes (e.g., 10 μL), the uncertainty in the calibration coefficients can be as high as $\pm 10\%$ due to insufficient sensor coverage by the calibration material. However, for sample volumes $\geq 35\ \mu L$, the uncertainties in coefficient values are $\leq \pm 1.5\%$ and are relatively independent of sample volume thereafter.

To calculate the dielectric constant based on the frequency-shift measurement obtained from a known sample volume of MUT, the positive roots of the polynomial in (7) are calculated using the calibration coefficients in Table II. Fig. 16 shows the extracted dielectric constants of 2-butyl alcohol, xylene, ethyl acetate, and ethylene glycol for sample volumes between 10–200 μL using the frequency shifts in Fig. 14(a) and the mean values of calibration coefficients. Since the uncertainties in calibration coefficients are very small especially for larger sample volumes, their exclusion does not significantly affect detection results.

TABLE II
CHEMICAL CALIBRATION COEFFICIENTS

S_v (μL)	$a(S_v)$	$b(S_v)$	$c(S_v)$
10	$-0.316 \pm 10.5\%$	$8.98 \pm 5.30\%$	$-8.67 \pm 5.10\%$
20	$-0.511 \pm 4.2\%$	$13.31 \pm 2.30\%$	$-12.80 \pm 2.20\%$
35	$-0.588 \pm 1.2\%$	$15.32 \pm 0.55\%$	$-14.59 \pm 0.56\%$
50	$-0.605 \pm 1.4\%$	$16.19 \pm 1.10\%$	$-15.59 \pm 1.10\%$
75	$-0.637 \pm 1.1\%$	$17.27 \pm 0.87\%$	$-16.63 \pm 0.86\%$
100	$-0.652 \pm 1.2\%$	$17.79 \pm 0.97\%$	$-17.14 \pm 0.97\%$
125	$-0.660 \pm 1.0\%$	$18.14 \pm 0.80\%$	$-17.48 \pm 0.80\%$
150	$-0.663 \pm 1.2\%$	$18.33 \pm 0.75\%$	$-17.66 \pm 0.73\%$
175	$-0.663 \pm 1.4\%$	$18.43 \pm 0.80\%$	$-17.77 \pm 0.77\%$
200	$-0.664 \pm 1.1\%$	$18.50 \pm 0.85\%$	$-17.83 \pm 0.85\%$

TABLE III
COLE–COLE-MODEL PARAMETERS FOR ORGANIC LIQUIDS AT 20 °C [13]

Organic liquid	ϵ_s	ϵ_∞	τ (ps)	α
Ethanol	25.07	4.5	143.24	0
Methanol	33.64	5.7	53.04	0
2-Butyl Alcohol	15.8	3.5	504	0
Xylene	2.53	2.27	9.55	0
Ethyl Acetate	6.04	2.48	4.34	0
Ethylene Glycol	38.7	2.6	106.1	0.1

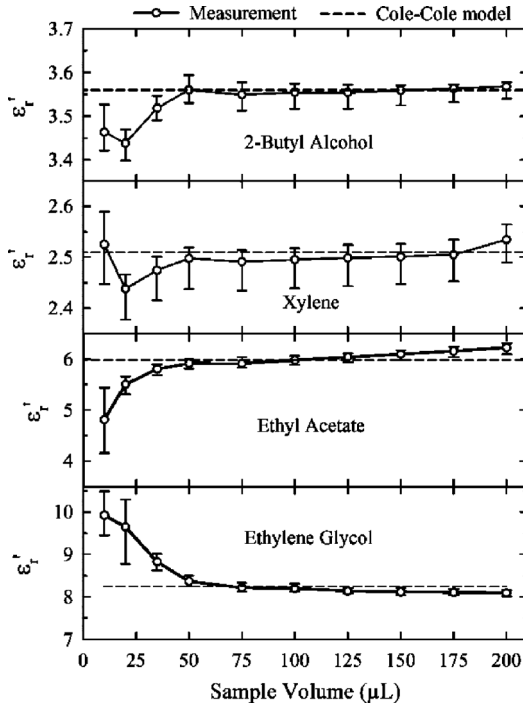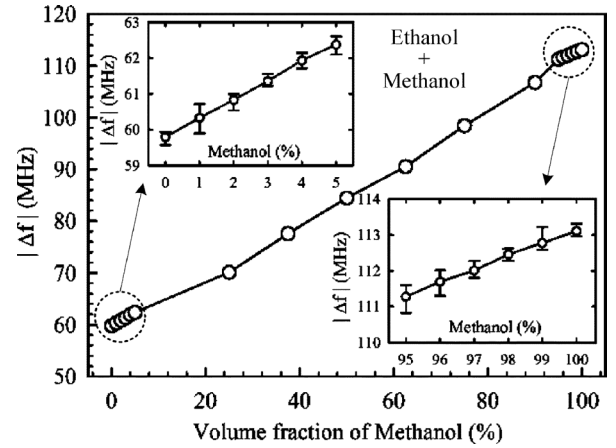Fig. 17. Frequency-shift measurements for ethanol–methanol mixtures.

Fig. 16. Measured dielectric-constant values of test materials at 4.5 GHz, as a function of sample volume.

The extracted values are compared to the theoretical values obtained from the single relaxation time-constant Cole–Cole model, which is expressed as [17]

$$\epsilon'_r(\omega) = \epsilon_\infty + \frac{\epsilon_s - \epsilon_\infty}{(1 + \omega^2\tau^2)^{(1-\alpha)}} \qquad (8)$$

where τ is the relaxation time, α is a fitting parameter, and ϵ_s and ϵ_∞ are the values of permittivity at angular frequencies $\omega \ll 1/\tau$ and $\omega \gg 1/\tau$, respectively. Table III shows the Cole–Cole-model parameters at 20 °C for the organic liquids tested in this work [13].

From Fig. 16, it is seen that insufficient sensor coverage results in inaccurate measurements for sample volumes $\leq 35~\mu$L, while the extracted ϵ'_r-value is relatively constant for sample volumes $> 35~\mu$L. Table IV shows the comparison between measured dielectric constants of test materials for sample volumes between 50–200 μL, and the theoretical value from the Cole–Cole equation at 4.5 GHz. The results are in excellent agreement and are independent of the ϵ''_r-values of these

materials which lie approximately between 0.1 (Xylene) and 13 (Methanol) at 4.5 GHz [13], thus proving the applicability of this system for dielectric-constant measurement of lossy liquid materials. The measured mean ϵ'_r-values are within $\pm4\%$ of the theoretical values with a maximum measurement uncertainity of $\pm2\%$. Some amount of measurement uncertainty can be attributed to frequency dependence of dielectric constant of the MUT whose impact can be estimated using (8). As the measurement frequency varies from 4.5 to 4.4 GHz, there is a maximum increase of only 2% in ϵ'_r for the materials listed in Table III. As a result, the assumption of frequency independence used in the simulation methodology in Section II.B is reasonably justified.

Compared to the free-running oscillator approach demonstrated in [12] where the measured ϵ'_r-value differs from the theoretical value by over 10%, the proposed method in this work allows increased accuracy of chemical calibration and detection due to use of higher sample volumes and accurate estimation of frequency shift due to digital averaging of loop filter output using the frequency synthesizer system.

D. Applicability to Dielectric Mixtures

Next, the ability of the system to distinguish between mixtures of two organic liquids is demonstrated. For this purpose, ethanol–methanol mixtures of various volume fractions were prepared by pipetting proportional volumes of liquids that need to be mixed into a test-tube and shaking them thoroughly to ensure a homogeneous solution. The frequency shift for each volume fraction of each mixture was measured five times for a sample volume of 100 μL, averaged and plotted versus volume fraction, as shown in Fig. 17. Here, a volume fraction of $x\%$ of one liquid implies that there is $(100 - x)\%$ of the other.

TABLE IV
EXTRACTED DIELECTRIC CONSTANTS OF ORGANIC MUTs FOR SAMPLE VOLUMES FROM 50 TO 200 μL

-	Theory	Measurements						
Organic MUT	Cole-Cole	50 μL	75 μL	100 μL	125 μL	150 μL	175 μL	200 μL
2-Butyl Alcohol	3.56	3.56 ± 0.033	3.55 ± 0.036	3.55 ± 0.038	3.55 ± 0.037	3.56 ± 0.033	3.56 ± 0.030	3.57 ± 0.028
Xylene	2.51	2.50 ± 0.060	2.49 ± 0.057	2.50 ± 0.056	2.50 ± 0.055	2.50 ± 0.054	2.51 ± 0.052	2.53 ± 0.044
Ethyl Acetate	5.98	5.92 ± 0.103	5.91 ± 0.124	5.98 ± 0.095	6.04 ± 0.103	6.09 ± 0.119	6.16 ± 0.121	6.22 ± 0.127
Ethylene Glycol	8.25	8.37 ± 0.129	8.22 ± 0.118	8.20 ± 0.115	8.14 ± 0.070	8.12 ± 0.093	8.11 ± 0.077	8.08 ± 0.071

Fig. 17(a) shows that the measured frequency shift is relatively linear with increasing volume fractions of methanol in an ethanol–methanol mixture. The system exhibits a sensitivity of around 0.53 MHz of frequency shift for every 1% increase in the volume fraction of methanol. The frequency resolution of this system is ultimately limited by systematic errors in sample volume dispensed and homogeniety of the sample mixture, and also random errors caused by oscillator phase noise and temperture fluctuations. An approximate estimation of frequency resolution of this system is obtained from the standard deviation of frequency shifts measured in Fig. 14, and is between 0.3–0.9 MHz for 50–200-μL sample volumes. The ability of the system to accurately estimate the volume fraction of constituent elements in a dielectric mixture has been successfully demonstrated.

V. CONCLUSION

A self-sustained low-cost microwave platform has been developed for dielectric-constant measurement of lossy organic liquids. Design of the oscillator for dielectric-constant measurement has been presented in detail. The use of a self-sustained frequency synthesizer system allows large sample volumes of lossy material to be tested, thereby providing large frequency shifts, which are then accurately measured using a unique detection algorithm. The extracted dielectric constant provides an accuracy better than $\pm 2\%$, and volume fractions of dielectric mixtures have been measured to around 1% accuracy.

REFERENCES

[1] K-.B. Kim, J.-H. Kim, S. S. Lee, and S. H. Noh, "Measurement of grain moisture content using microwave attenuation at 10.5 GHz and moisture density," *IEEE Trans. Instrum. Meas.*, vol. 51, no. 1, pp. 72–77, Feb. 2002.

[2] H. M. A. Al-Mattarneh, D. K. Ghodgaonkar, and W. M. M. A. Majid, "Microwave nondestructive testing for classification of Malaysian timber using free-space techniques," in *6th Int. Signal Process. and Its Appl. Symp.*, Kuala Lumpur, Malaysia, 2001, vol. 2, pp. 450–453.

[3] S. Gabriel, R. W. Lau, and C. Gabriel, "The dielectric properties of biological tissues: II. Measurements in the frequency range 10 Hz to 20 GHz," *Phys. Med. Biol.*, vol. 41, pp. 2251–2269, 1996.

[4] G. Smith, A. P. Duffy, J. Shen, and C. J. Olliff, "Dielectric relaxtion spectroscopy and some applications in the pharmaceutical sciences," *J. Pharmaceut. Sci.*, vol. 84, no. 9, pp. 1029–1044, Sep. 1995.

[5] E. J. Vanzura, R. G. Geyer, and M. D. Janezic, "The NIST 60-millimeter diameter cylindrical cavity resonator: Performance evaluation for permittivity measurements," NIST, Boulder, CO, Tech. Note 1354, Aug. 1993.

[6] K. Saeed, R. D. Pollard, and I. C. Hunter, "Substrate integrated waveguide cavity resonators for complex permittivity characterization of materials," *IEEE Trans. Microw. Theory Tech.*, vol. 56, no. 10, pp. 2340–2347, Oct. 2008.

[7] P. A. Bernard and J. M. Gautray, "Measurement of dielectric constant using a microstrip ring resonator," *IEEE Trans. Microw. Theory Tech.*, vol. 39, no. 3, pp. 592–595, Mar. 1991.

[8] E. Fratticcioli, M. Dionigi, and R. Sorrentino, "A simple and low-cost measurement system for the complex permittivity characterization of materials," *IEEE Trans. Microw. Theory Tech.*, vol. 53, no. 4, pp. 1071–1077, Apr. 2004.

[9] W. Ho, G. M. Hidy, and R. M. Govan, "Microwave measurements of the liquid water content of atmospheric aerosols," *J. Appl. Meteorol.*, vol. 13, pp. 871–879, Dec. 1974.

[10] P. G. Wilson and R. D. Carver, "An easy-to-use FET DRO design procedure suited to most CAD programs," in *IEEE MTT-S Microw. Symp. Dig.*, Jun. 1999, vol. 3, pp. 1033–1036.

[11] H-.J. Lee and J-.G. Yook, "Biosensing using split-ring resonators at microwave regime," *Appl. Phys. Lett.*, vol. 92, 2008, Art. ID 254103.

[12] V. Sekar, W. J. Torke, S. Palermo, and K. Entesari, "A novel approach for dielectric constant measurement using microwave oscillations," in *IEEE MTT-S Int. Microw. Symp. Dig.*, Jun. 2011, pp. 1–4.

[13] F. Buckley and A. A. Maryott, "Tables of dielectric dispersion data for pure liquids and dilute solutions" NIST, Boulder, CO, 1958, NBS Circular 589.

[14] "ADF4157 data sheet," Analog Devices Inc., Norwood, MA, Rev. A ed., 2007.

[15] "C8051F060/1/2/3/4/5/6/7 data sheet," Silicon Labs. Inc., Austin, TX, Prelim. Rev. 1.2, 2004.

[16] A. P. Gregory and R. N. Clarke, "Tables of complex permittivity of dielectric reference liquids at frequencies up to 5 GHz," NPL, Middlesex, U.K., Rep. CETM 33, Sep. 2001.

[17] K. S. Cole and R. H. Cole, "Dispersion and absorption in dielectrics I: Alternating current characteristics," *J. Chem. Phys.*, vol. 9, no. 4, pp. 341–351, Apr. 1941.

[18] G. S. P. Castle and J. Roberts, "A microwave instrument for the continuous monitoring of the water content of crude oil," *Proc. IEEE*, vol. 62, no. 1, pp. 103–108, Jan. 1974.

[19] S. Palermo, "A multi-band phase-locked loop frequency synthesizer," M.S. thesis, Dept. Elect. Comput. Eng., Texas A&M Univ., College Station, TX, 1999, pp. 36–41.

[20] F. Garner, *Phaselock Techniques*, 3rd ed. Hoboken, NJ: Wiley, 2005.

[21] G. R. Cooper and C. D. McGillem, *Probabilistic Methods of Signal and System Analysis*, 2nd ed. New York: Harcourt Brace Johanovich, 1986.

Vikram Sekar (S'07–M'12) received the Bachelors degree in electrical engineering from Visveswariah Technological University, Belgaum, India, in 2006, and the M.S. and Ph.D. degrees in electrical engineering from Texas A&M University, College Station, in 2008 and 2011, respectively.

During the summers of 2007 and 2008 he was an Intern with Texas Instruments Incorporated, Dallas, TX, where he was involved with signal integrity and crosstalk in wireless handsets. He is currently an Electromagnetic Modeling Engineer with Peregrine Semiconductor, San Diego, CA, where he is involved with the development of device and package models for UltraCMOS silicon-on-sapphire technology. His research interests include microwave filters, nonlinearity and noise in tunable filters, RF microelectromechanical systems, and microwave sensors.

Dr. Sekar was the recipient of the Third Place Award of the 2011 IEEE Microwave Theory and Techniques Society (IEEE MTT-S) International Microwave Symposium (IMS) Student Paper Competition.

William J. Torke (S'11) received the B.S. degree in electrical engineering from Purdue University, West Lafayette, IN, in 1995, and the M.Sc. degree in electrical engineering from Texas A&M University, College Station, in 2011. His primary M.Sc. research topic pertained to PLLs.

During his undergraduate study, he was also a co-op employee with Thomson Consumer Electronics. He has been with several companies in Austin, TX including AMD, Cygnal Integrated Products Inc. (since acquired by Silicon Laboratories Inc.), and Cirrus Logic Inc. He has primarily been an Applications Engineer supporting power metering and microcontroller IC products, and also a Software/Firmware Engineer. He is currently an Analog Hardware Engineer with National Instruments, Austin, TX.

Mr. Torke was the recipient of the 2009 Hardy Caton Fellowship.

Samuel Palermo (S'98–M'08) received the B.S. and M.S. degrees in electrical engineering from Texas A&M University, College Station, in 1997 and 1999, respectively, and the Ph.D. degree in electrical engineering from Stanford University, Stanford, CA, in 2007.

From 1999 to 2000, he was with Texas Instruments Incorporated, Dallas, TX, where he was involved with the design of mixed-signal ICs for high-speed serial-data communication. From 2006 to 2008, he was with the Intel Corporation, Hillsboro, OR, where he was involved with high-speed optical and electrical I/O architectures. In 2009, he joined the Electrical and Computer Engineering Department, Texas A&M University, where he is currently an Assistant Professor. His research interests include high-speed electrical and optical links, clock recovery systems, and techniques for device variability compensation.

Dr. Palermo is a member of Eta Kappa Nu. He was a corecipient of the Jack Raper Award for Outstanding Technology-Directions Paper of the 2009 International Solid-State Circuits Conference.

Kamran Entesari (S'03–M'06) received the B.S. degree in electrical engineering from the Sharif University of Technology, Tehran, Iran, in 1995, the M.S. degree in electrical engineering from Tehran Polytechnic University, Tehran, Iran, in 1999, and the Ph.D. degree from The University of Michigan at Ann Arbor, in 2005.

In 2006, he joined the Department of Electrical and Computer Engineering, Texas A&M University, College Station, where he is currently an Assistant Professor. His research interests include design of RF/microwave/millimeter-wave ICs and systems, RF microelectromechanical systems (MEMS), and medical electronics.

Dr. Entesari was the recipient of the 2011 National Science Foundation (NSF) CAREER Award. He was a corecipient of the 2009 Semiconductor Research Corporation (SRC) Design Contest Second Project Award for his work on dual-band millimeter-wave receivers on silicon.